

## A multifunctional layered photonic structure with NOR logical operation and multiscale detection based on the PT-symmetry breaking

Rui-yang Dong, Jun-yang Sui, You-Ran Wu, Jing-Yi Liu & Hai-feng Zhang

To cite this article: Rui-yang Dong, Jun-yang Sui, You-Ran Wu, Jing-Yi Liu & Hai-feng Zhang (2023): A multifunctional layered photonic structure with NOR logical operation and multiscale detection based on the PT-symmetry breaking, *Waves in Random and Complex Media*, DOI: [10.1080/17455030.2023.2234055](https://doi.org/10.1080/17455030.2023.2234055)

To link to this article: <https://doi.org/10.1080/17455030.2023.2234055>



Published online: 12 Jul 2023.



Submit your article to this journal [↗](#)



View related articles [↗](#)



View Crossmark data [↗](#)



# A multifunctional layered photonic structure with NOR logical operation and multiscale detection based on the PT-symmetry breaking

Rui-yang Dong<sup>a</sup>, Jun-yang Sui<sup>b</sup>, You-Ran Wu<sup>b</sup>, Jing-Yi Liu<sup>a</sup> and Hai-feng Zhang<sup>b</sup>

<sup>a</sup>Bell Honors School & Intensive courses in science and engineering, Nanjing University of Posts and Telecommunications, Nanjing, People's Republic of China; <sup>b</sup>College of Electronic and Optical Engineering & College of Flexible Electronics (Future Technology), Nanjing University of Posts and Telecommunications, Nanjing, People's Republic of China

## ABSTRACT

In this paper, a multifunctional layered photonic structure (LPS) with NOR logical operation and multiscale detection based on the parity-time (PT) symmetry breaking composed of magnetized yttrium iron garnet (YIG) is proposed in theory. The accurate NOR logical operation is completed by properly modulating the target resonant absorption peak (AP) by the external magnetic field and using the peak to ascertain the logical operation. Given the high-quality factor of the resulting APs, the proposed structure can be used to detect four important physical quantities, which are angle, magnetic field, the thickness of ferrite<sub>1</sub>, and refractive index (RI). YIG is a typical representative of ferrite. Due to the magneto-optical effect, the PT-symmetry is broken, resulting in a nonreciprocal phenomenon, thereby further realizing NOR logic operation and multi-physical quantity detection on the front and rear scales. Since the RI of YIG is modulated by the magnetic field, the change of the magnetic field can cause the AP generated by the resonance to shift, so that the magnetic field can be detected.

## ARTICLE HISTORY

Received 14 November 2022  
Accepted 3 July 2023

## KEYWORDS


Layered photonic structure;  
PT-symmetry; Logical  
operation; Detection;  
Multiscale devices

## 1. Introduction

The one-dimensional (1-D) layered photonic structure (LPS) [1] is a typical representative of photonic crystals (PCs) [2,3]. Because it has some excellent characteristics for controlling electromagnetic waves (EWs) [4], it is still the focus of research. The LPS has two essential properties, the photonic band gaps (PBGs) [5] and the strong photon confinement result [6]. So, it is often used to make logic operation controls [7], sensors [8,9], waveguides [10], and filters [10].

Due to the magneto-optical properties of yttrium iron garnet (YIG), the permeability of YIG is tensor under the action of an external magnetic field [11,12]. The permeability tensor will be changed under the transverse and longitudinal magnetization configuration. Of

**CONTACT** Hai-feng Zhang ✉ [hanlor@njupt.edu.cn](mailto:hanlor@njupt.edu.cn)

 Supplemental data for this article can be accessed here. <https://doi.org/10.1080/17455030.2023.2234055>

course, this perfect magnetic tunability makes YIG a hot spot [13–15]. This anisotropy allows YIG to be used for the preparation of optical filters [16,17], optical circulators [18,19], and so on.

On the other hand, the parity-time (PT) symmetry breaking of LPS will greatly improve the potential physical application value. Their simplest implementation is two identical coupled waveguides, one with gain and the other with loss, so that the real part of the RI is symmetrical with respect to the exchange of the waveguides. The interchange of the waveguides, while the corresponding part of the imaginary numbers is asymmetric [20,21]. In an optical system, a PT-symmetry breaking can be simplified to mean that EWs show different transmission, reflection, absorption, or other characteristics when they propagate forward and backward. In fact, some potential effects can be observed even without gain, although when both waveguides contain unequal losses [22]. This has been demonstrated in previous experiments [23]. Based on this experiment it is possible to explain how our structure breaks the PT – symmetry. Since YIG is an anisotropic material, the loss when the EW propagates from the forward direction is not the same as the loss when it propagates from the reverse direction, and the phenomenon brought about by the broken PT-symmetry can be observed even without gain. The insertion of YIG into the proposed periodic structure smashes the structural symmetry, and the time symmetry is destructed because the permeability of the YIG is regulated by an external magnetic field. Therefore, through positioning absorption peak (AP), the proposed LPS in this paper implements forward and backward NOR logical operation at different frequency points and multi-physical detection.

In recent years, a logical operation is more and more widely used in communication, computers, and other fields. Many of them are devoted to the study of logical operation. He *et al.* committed themselves to research filters and logical gates based on two-dimensional LPS with stable edge states, achieving logical gates like OR, AND, and XNOR utilizing linear interference [24]. Zou *et al.* suggested a 1-D photonic heterostructure for all-optical logical gates, half adders, and double switches with great efficiency [25]. Wang *et al.* researched a high-sensitivity PCs refractive index sensor-based defect mode [26]. It had a linear measurement range of 1.45-1.46 and a sensitivity of 28,000 nm/RIU. Most of the studies mentioned above can only achieve one function and fail to be applied in multiple scenarios. Only focus on the improvement of a single performance, which to a certain extent limits the research ideas in the field of reform. The electromagnetic device with multi-function and multi-scale will meet the needs of more scenes, with great research value and development prospects.

Considering the above problems and requirements, this paper proposes a multifunctional LPS with the magnetic-controlled NOR logical operation and multiscale detection based on the PT-symmetry breaking composed of magnetized YIG layers. In the terahertz (THz) range, this LPS can realize the functions of logical operation and detection simultaneously. Specifically, located by AP, it is possible to accomplish NOR logical operation and forward angle, YIG thickness, refractive index (RI) detection, and detection of backward  $H_{01}$  and  $H_{02}$  magnetic field small changes. The detection of multi-physical quantities is due to the realization of the PT-symmetry breaking. In addition, the important metrics to consider when evaluating a detection are sensitivity (S), quality factor (Q), the figure of merit (FOM), and the detection limit (DL). The detection ranges of multi-physical quantities are also highlights of this paper. It should be emphasized that this article predominantly focuses on

theoretical research, an experiment that is without in the scope of this work, and is expected to be reflected in future work.

## 2. Design and discussion

### 2.1. Theoretical model and simulation

The diagram of the proposed 1-D LPS is plotted in Figure 1. The different colored squares are represented different dielectrics. To better apply to the general situation, the whole structure is exposed to the air.  $\theta$  is the incident angle. When the EWs travel through this 1-D LPS, the Lorentz force affects EWs with TE polarization but not EWs with TM one [11]. TE and TM polarization can be written as [11]

$$\eta_{TE} = \sqrt{\frac{\varepsilon_0}{\mu_0}} \sqrt{\varepsilon} \cos \theta \quad (1)$$

$$\eta_{TM} = \sqrt{\frac{\varepsilon_0}{\mu_0}} \frac{\sqrt{\varepsilon}}{\cos \theta} \quad (2)$$

As a result, the applied magnetic field only has a controlling influence on TE polarization [27]. Hence, this work will concentrate on the magnetic control performance under TE polarization cases. Red arrows and blue arrows indicate EWs incident from the front and back, respectively. A single A layer and B layer improve the value of A. The whole structure is asymmetric and magnetic field intensity  $H_{01}$  and  $H_{02}$  are externally applied magnetic fields along the y-axis, so the PT-symmetry of LPS can be broken. The same or even more complex magnetic field distribution can be found in Ref. [28,29]. Consequently, the non-reciprocal property of YIG is formed, achieving the function of the forward and backward magnetic-controlled NOR logical operation and the detection of multi-physical quantities. Moreover, the thicknesses of the dielectrics A, B, C, and D are denoted by  $d_A$ ,  $d_B$ ,  $d_C$ , and  $d_D$ , while  $d_A = 25 \mu\text{m}$ ,  $d_B = 35 \mu\text{m}$ ,  $d_C = 25 \mu\text{m}$ , and  $d_D = 55 \mu\text{m}$ .  $d_1$  and  $d_2$  are employed to simplify the thicknesses of YIG<sub>1</sub> and YIG<sub>2</sub>, which are set as  $d_1 = 1.9 \mu\text{m}$  and  $d_2 = 1.5 \mu\text{m}$ . The RI of dielectrics are fixed to  $n_A = 3.5$ ,  $n_B = 2.7$ ,  $n_C = 3.853$ , and  $n_D = 2.45$ . Both Ferrite<sub>1</sub> and

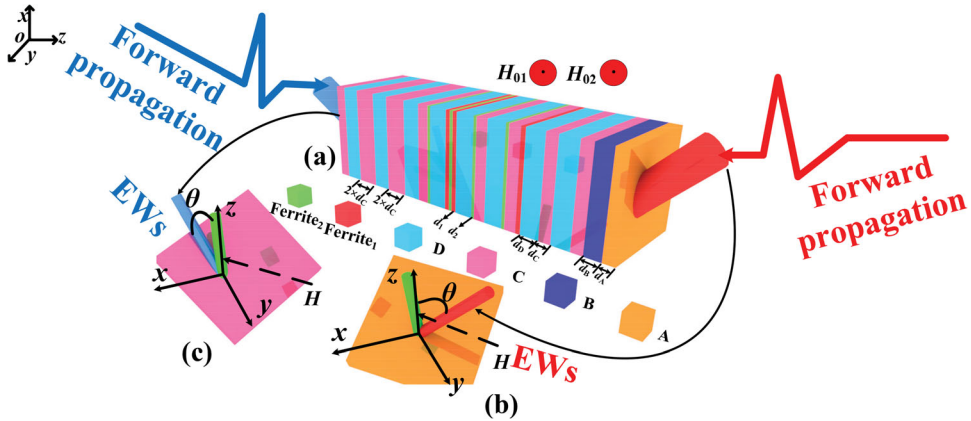


**Figure 1.** a) The illustration of the proposed LPS, b) the forward propagation, and c) the backward propagation.

Ferrite<sub>2</sub> are made up of YIG<sub>1</sub> and YIG<sub>2</sub>, but each YIG layer has a different external magnetic field strength. The permittivities of the YIG layers are  $\varepsilon_1 = \varepsilon_2 = 15$  [30]. The transmission characteristics of the whole structure are calculated using the transfer matrix method [31]. The parameters of the above structure are optimized.

For YIG, under the influence of an external magnetic field, the effective permittivity of YIG appears as a tensor form. The expression for the YIG tensor and specific components is as followed [32]

$$\boldsymbol{\mu}_m = \begin{pmatrix} \mu_r & 0 & j\mu_k \\ 0 & \mu_0 & 0 \\ -j\mu_k & 0 & \mu_r \end{pmatrix} \quad (3)$$

$$\mu_r = 1 + \frac{\omega_m(\omega_0 - j\alpha\omega)}{(\omega_0 - j\alpha\omega)^2 - \omega^2} \quad (4)$$

$$\mu_k = \frac{\omega_m\omega}{(\omega_0 - j\alpha\omega)^2 - \omega^2} \quad (5)$$

where  $\omega_m = 2\pi\gamma M_s$  represents the circular frequency of YIG.  $\gamma = 2.8 \text{ GHz}\cdot\text{Oe}^{-1}$  [26] is the gyromagnetic ration and  $M_s = 1780\text{Oe}$  [26] is the saturation magnetization.  $\omega_0 = 2\pi\gamma H_0$  is the resonance frequency, where  $H_0$  is the magnetic strength.  $\alpha = 0.02$  is the damping coefficient [31]. The effective RI of YIG is [30]

$$n_{YIG} = \sqrt{(\mu_r^2 + (j\mu_k)^2)\varepsilon_m/\mu_r} \quad (6)$$

According to Maxwell's equations and the boundary conditions, the deduced transfer matrix is followed [30]

$$\mathbf{M}_{TE} = \begin{pmatrix} \cos(k_{TE}d_i) + \sin(k_{TE}d_i) \frac{k_{TEy}\mu_k}{k_{TE}x\mu_r} & -\frac{j}{\eta_{TE}} \left[ 1 + \left( \frac{k_{TEy}\mu_k}{k_{TE}x\mu_r} \right)^2 \right] \sin(k_{TE}d_i) \\ -j\eta_{TE}\sin(k_{TE}d_i) & \cos(k_{TE}d_i) - \sin(k_{TE}d_i) \frac{k_{TEy}\mu_k}{k_{TE}x\mu_r} \end{pmatrix} \quad (7)$$

where YIG<sub>1</sub> and YIG<sub>2</sub> are stated by  $i$  denoting 1 and 2, respectively.  $k_{TE} = (\omega/c) \cdot (\varepsilon_m/\mu_r) \cdot (\mu_r^2 + (j\mu_k)^2)^{1/2}$ ,  $\eta_{TE} = (\mu_0/\varepsilon_0)^{1/2} \cdot ((\mu_r^2 + (j\mu_k)^2)/(\varepsilon_m \cdot \mu_r))^{1/2} / \cos\theta_f$ ,  $k_{TEy} = k_{TE} \cdot \sin\theta_f$ ,  $k_{TE}x = k_{TE} \cdot \cos\theta_f$ , and  $\theta_f$  is the incident angle of lights into YIG layers.

The transfer matrix of an ordinary dielectric layer is [31]

$$\mathbf{M}_i = \begin{pmatrix} \cos \delta_i & -j \sin \delta_i / \eta_i \\ -j \eta_i \sin \delta_i & \cos \delta_i \end{pmatrix} \quad (8)$$

where the subscript  $i$  can represent 1, 2, 3, and 4 denoting dielectric layers A, B, C, and D.  $\delta_i = n_i \cdot d_i \cdot \cos\theta_i \cdot (2\pi/\lambda)$  and  $\eta_i = (\varepsilon_0/\mu_0)^{1/2} \cdot n_i \cdot \cos\theta$ . And  $\mathbf{M}_f$  is the forward scale transfer matrix while  $\mathbf{M}_b$  is the backward scale. The specific expressions of A and B are as

follows [33]

$$\mathbf{M}_f = \mathbf{M}_A \mathbf{M}_B (\mathbf{M}_C \mathbf{M}_D)^2 \mathbf{M}_1 (\mathbf{M}_C \mathbf{M}_2 \mathbf{M}_D)^2 \mathbf{M}_1 \mathbf{M}_2 \mathbf{M}_1 \mathbf{M}_D \mathbf{M}_2 (\mathbf{M}_C \mathbf{M}_D \mathbf{M}_C)^3 \quad (9)$$

$$\mathbf{M}_b = (\mathbf{M}_C \mathbf{M}_D \mathbf{M}_C)^3 \mathbf{M}_2 \mathbf{M}_D \mathbf{M}_1 \mathbf{M}_2 \mathbf{M}_1 (\mathbf{M}_D \mathbf{M}_2 \mathbf{M}_C)^2 \mathbf{M}_1 (\mathbf{M}_D \mathbf{M}_C)^2 \mathbf{M}_B \mathbf{M}_A \quad (10)$$

where  $\mathbf{M}_A$ ,  $\mathbf{M}_B$ ,  $\mathbf{M}_C$ , and  $\mathbf{M}_D$  stand for the transfer metrics of dielectrics A, B, C, and D.  $\mathbf{M}_1$  and  $\mathbf{M}_2$  denote the transfer metrics of YIG<sub>1</sub> and YIG<sub>2</sub>, respectively.

At the same time, to obtain the absorption rate, we need to first calculate the transmittance and reflectance, whose calculation formulas are [31]

$$r = \frac{(m_{11} + m_{12}\eta_{N+1})\eta_0 - (m_{11} + m_{12}\eta_{N+1})}{(m_{11} + m_{12}\eta_{N+1})\eta_0 + (m_{11} + m_{12}\eta_{N+1})} \quad (11)$$

$$t = \frac{2\eta_0}{(m_{11} + m_{12}\eta_{N+1})\eta_0 + (m_{11} + m_{12}\eta_{N+1})} \quad (12)$$

$$R = |r|^2 \quad (13)$$

$$T = |t|^2 \quad (14)$$

where  $\eta_0 = \eta_{N+1} = (\epsilon_0/\mu_0)^{1/2} \cdot \cos\theta_f$ . Thus, the absorption rate can be easily obtained, and its formula is

$$A = 1 - R - T \quad (15)$$

## 2.2. NOR logical operation

The following will be a more detailed explanation of the physical phenomena and functional analysis of the NOR logical operation. In Figure 2a, it can be found that the  $T$  of the whole structure is 0, meaning the formation of PBG. When frequency = 8.391 THz, the  $R$  decreases rapidly, while the  $A$  increases rapidly at the position corresponding to the frequency point in Figure 2b. This is in full agreement with the theory. Considering two externally applied different magnetic fields as two different input logical energy levels,  $H_{01}$  is used as the first input logical energy level ( $I_1$ ) while  $H_{02}$  is the second input logical energy level ( $I_2$ ). At the same time, when the AP ( $A > 0.9$ ) appears, the result of the output logical operation is 1, otherwise, the output logical operation ( $A < 0.1$ ) is 0. Here, we only care about  $A$  at the corresponding frequency point when performing logical transformation operations, and do not care about  $A$  at other frequencies. This ensures a more accurate modulation of the magnetic field for logic operations. This can ensure a more accurate magnetic field modulation of the logical operation. In Figure 2b, when both external magnetic fields are absent ( $H_{01} = 0$  Oe and  $H_{02} = 0$  Oe), it means that the first and second input energy levels are 0. Meanwhile, the output logical operation is 1, because of the occurrence of an  $A$  greater than 0.9. The values of frequency and  $A$  are 8.391 THz and 0.941, respectively. Then, when the external magnetic field  $H_{01}$  exists but  $H_{02}$  does not ( $H_{01} = 1350$  Oe and  $H_{02} = 0$  Oe), the first input energy level is 1 and the second input level is 0. Only the  $A$  with a value of 0.15 appears while the frequency = 8.392 THz is not equal to the previous case frequency = 8.391 THz and the output logical operation is 0. This situation is also suitable for NOR logic operation. Next, when the external magnetic field  $H_{02}$  occurs but  $H_{01}$  disappears ( $H_{01} = 0$  Oe and  $H_{02} = 4400$  Oe), it is the opposite of the previous case. The first

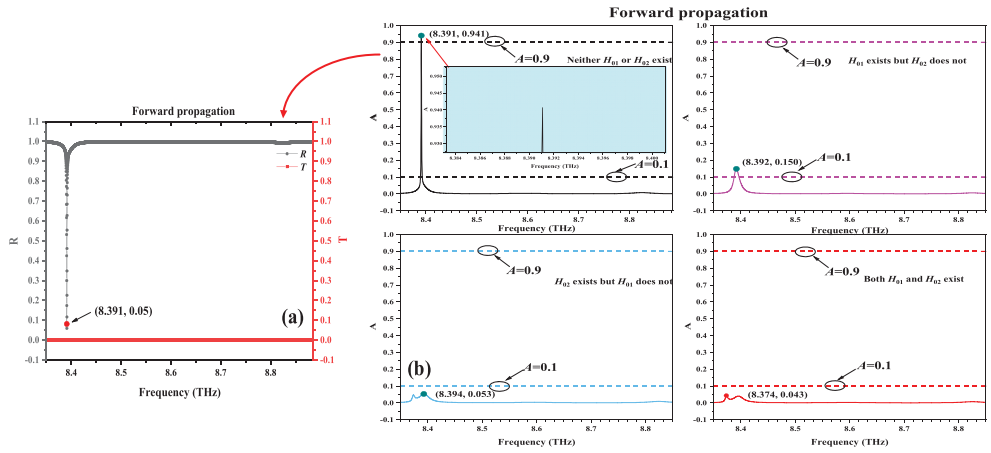


**Figure 2.** Schematic diagrams of (a)  $R$  and  $T$ , (b) logical operation of forward magnetic field modulation.

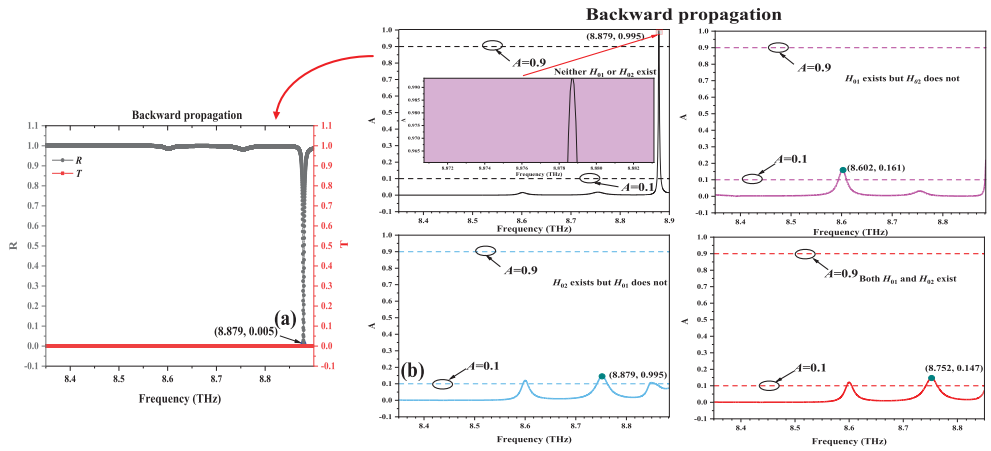


**Figure 3.** Illustration of (a)  $R$  and  $T$ , (b) logical operation of backward magnetic field modulation.

input energy level is 0 and the second input level is 1. The magnitude of the maximum  $A$  is less than 0.1, which reaches 0.053 at the frequency of 8.394 THz, and the output logical operation is 0. Finally, both  $H_{01}$  and  $H_{02}$  exist ( $H_{01} = 1350$  Oe and  $H_{02} = 4400$  Oe), corresponding to the first input energy level and the second input level of 1. At this point, the  $A$  is also less than 0.1, only 0.043 when the frequency is 8.374 THz. In this case, the output logical operation is 0. Based on the above analysis, the results obtained by LPS can be well in line with the NOR logic operation and form an accurate magnetic field modulation. From the absence of a magnetic field to the presence of a magnetic field, this will be taken into account later in the magnetic field detection.

To understand the NOR logic operation more intuitively and clearly, the truth table is shown in Table 1. '  $I_1$  ' and '  $I_2$  ' correspond to the first and second input energy levels, respectively. '  $O$  ' indicates the output logical operation. Figure 3 shows the backward NOR logic operation, and the analysis is similar to the forward propagation in Figure 2. The value of  $A$  is equal to 0.995 at the frequency of 8.879 THz when neither  $H_{01}$  nor  $H_{02}$  exists.

**Table 1.** Truth table of the NOR logical operation (the input energy level and output logic operation is shown in parentheses).

$I_1$	$I_2$	O
0	0	1 ( $A > 0.9$ )
1 ( $H_{01}$ exists)	0	0 ( $A < 0.1$ )
0	1 ( $H_{02}$ exists)	0 ( $A < 0.1$ )
1 ( $H_{01}$ exists)	1 ( $H_{02}$ exists)	0 ( $A < 0.1$ )

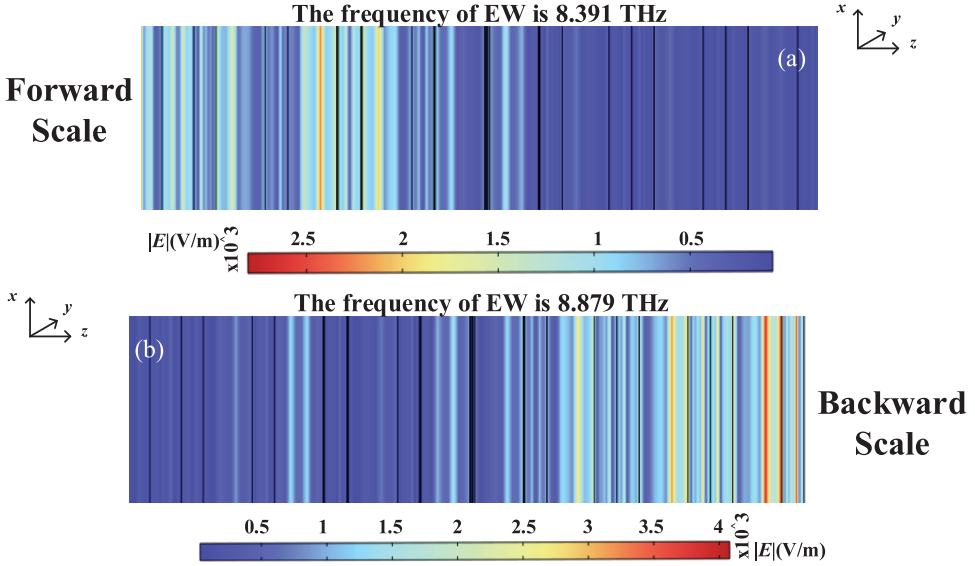


**Figure 4.** The charts of the electric field distributions, (a) the forward scale, and (b) the backward scale.

To understand the mechanism of the formation of a high AP, the forward and backward electric field distributions are plotted in Figure 4. Considering the asymmetry of the proposed structure and the application of two external magnetic fields to break the PT-symmetry, the non-reciprocal phenomenon is formed. As exhibited in Figure 4(a), the AP appears at a frequency of 8.391 THz. Since the YIG layer is introduced into the periodic structures A, B, C, and D, it can be clearly and intuitively seen from Figure 4(a) that the energy is localized in the YIG layer close to the propagation direction. It turns out that when the frequency of the EWs is the natural frequency of the YIG layer of the LPS, resonance will happen and the electrons will vibrate violently, resulting in high electric field energy in the YIG layer. Meanwhile, in the YIG layer, the forward incident EWs will interact with the backward reflected EWs again to produce a destructive interference effect, continuing to increase the electric field energy. A highly resonant AP is generated here. However, in the back part of the LPS, the electric field diagram is demonstrated in blue. This means that the EWs do not pass through the LPS. The analysis of the forward propagation is also applicable to Figure 4(b) (the backward case). Therefore, through accurate magnetic field modulation, the logical operation can be well realized by the precise positioning of AP.

As shown in Figure 5 (a), (b), and (c), we also show the electric field distributions with output logic operation 0 in forward propagation under the condition of  $H_{01}$  exists but  $H_{02}$



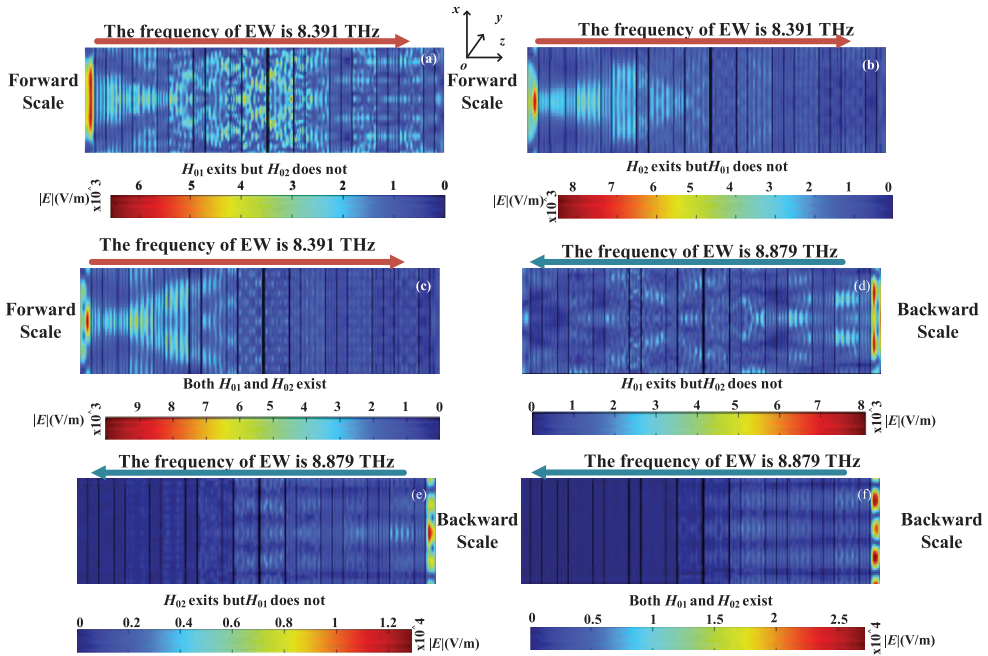


**Figure 5.** Graphs of the electric field distribution. Forward EWs go through the LPS when frequency is 8.391 THz: (a)  $H_{01}$  exists but  $H_{02}$  does not. (b)  $H_{02}$  exists but  $H_{01}$  does not. (c) Both  $H_{01}$  and  $H_{02}$  exist. Backward EWs go through the LPS when frequency is 8.879 THz: (d)  $H_{01}$  exists but  $H_{02}$  does not. (e)  $H_{02}$  exists but  $H_{01}$  does not. (f) Both  $H_{01}$  and  $H_{02}$  exist.

does not,  $H_{02}$  exists but  $H_{01}$  does not, and both  $H_{01}$  and  $H_{02}$  exist, apart. In front of LPS is the air layer. It is obvious that the energy is concentrated in the air layer in front of the LPS. The EWs do not enter the LPS, and a huge part of the energy is reflected out, so there is no sharp AP in the LPS, which corresponds to the  $A = 0$  in Figure 2. The electric field distributions of the backward scale are displayed in Figure 5 (d), (e), and (f) in the case of  $H_{01}$  exists but  $H_{02}$  does not,  $H_{02}$  exists but  $H_{01}$  does not, both  $H_{01}$  and  $H_{02}$  exist, separately. Similarly, an air layer is also added at the end of the structure. The electric field distributions for forward propagation and backward propagation are similar. Most of the electric field is forced on the air layer, and there are no EWs passing through the LPS. These results are in perfect agreement with the results in Figure 3 that there is no AP in the LPS. Based on the above analysis, it is proved and explained that sharp AP can appear in the LPS only when  $H_{01}$  and  $H_{02}$  do not exist, forming the NOR logical operation of precise magnetic field regulation.

In Figure 6, the  $A$  of three-dimensional (3-D) maps at the range of  $0^\circ \sim 25^\circ$  are plotted. At the top of the layer is a 3-D graph of  $A$  varying with  $\theta$  and frequency, and at the bottom is a plane view from the 3-D view. In Figure 6(a), from the 3-D graph, the AP of forward propagation is always higher than 0.9 within a given range of angles around  $0^\circ \sim 25^\circ$ . At the same time, it can be seen from the planar picture that with the increase of  $\theta$ , the blue-shift phenomenon of AP occurs, that is, gradually moving to the high frequency. However, in Figure 6(b), the  $A$  of the backward scale is higher than 0.9 only within the scope of  $0 \sim 20^\circ$  while in the range of  $20^\circ \sim 25^\circ$ , the  $A$  fall below 0.9, which fails to meet the requirement of logical operation. Similar to Figure 6(a), with the change of  $\theta$ , the AP has a blue-shift.

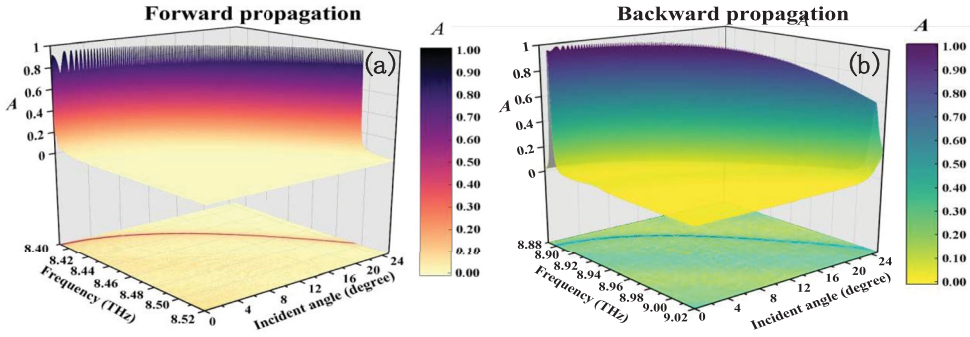


**Figure 6.** The  $A$  of 3-D map at the range of  $0^\circ \sim 25^\circ$ . (a) Forward scale. (b) Backward scale.

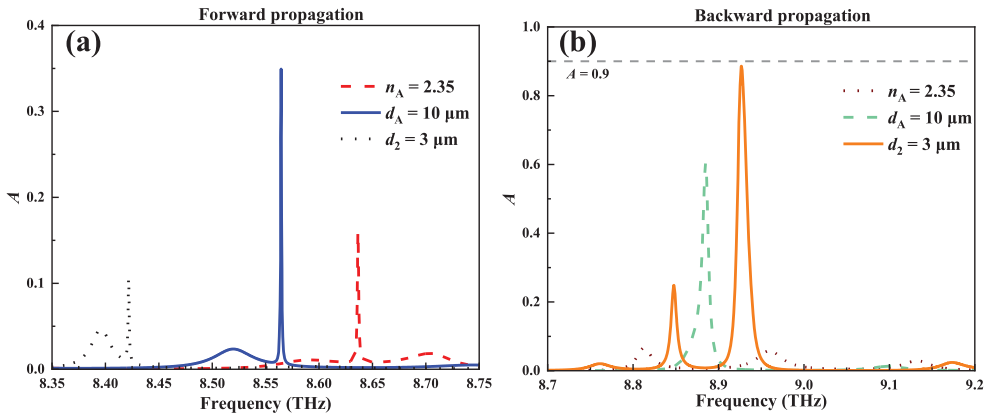


**Figure 7.** The values of  $A$  for different parameters:  $n_A = 2.35$ ,  $d_A = 10 \mu\text{m}$ , and  $d_2 = 3 \mu\text{m}$ . (a) Forward propagation. (b) Backward propagation.

Therefore, the angular stability of NOR logical operation performance is  $20^\circ$ . This specialty can make logical operations have a greater practical application.

Moreover, to verify that the logical operation is precisely magnetic field controlled, more parameters are discussed in Figure 7, including  $n_A$ ,  $d_A$ , and  $d_2$ . When these parameters are varied, the values of  $A$  forward and backward scales are all obviously less than 0.9, which is completely out of line with the basic requirements for NOR logic operation. Hence, the NOR logic operation is precisely controlled by  $H_{01}$  and  $H_{02}$ . This has a great application prospect in devices requiring high precision.

### 2.3. Detector

In past studies, many researchers attached great importance to improving the detector performance but ignored the detection of multiple physical quantities. This research idea limits the development of detectors to a certain extent. In this paper, we break down the PT-symmetry of the LPS. Therefore, we can realize forward and backward multi-physics detection at the same time.

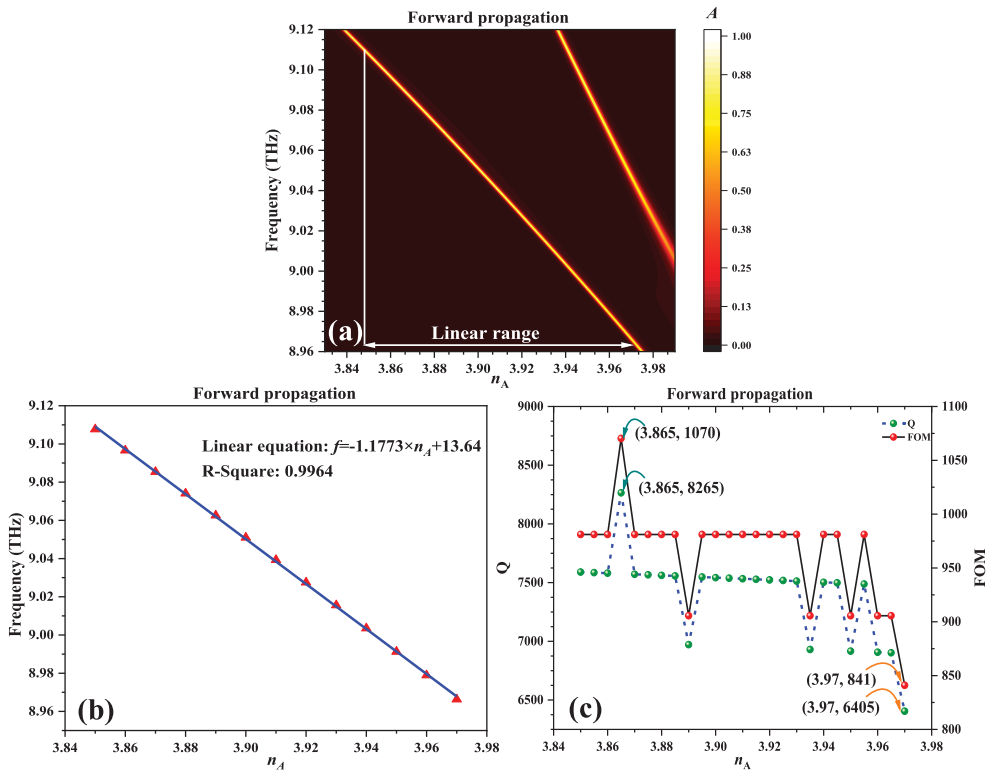


**Figure 8.** (a) The 3-D top view of the  $A$  vary with  $n_A$  and frequency. (b) The linear fitting equation between  $n_A$  and frequency. (c)  $Q$  and FOM variation with  $n_A$ .

Important metrics to consider when evaluating a detection are  $S$ ,  $Q$ , FOM, and DL. A good detection has a greater  $S$ , a higher  $Q$ , a higher FOM, and a lower DL. The definitions are given as follows, where  $\Delta f$  and  $\Delta n$  denote frequency and RI change, respectively, while  $f_T$  denotes the resonant frequency and full width at half maxima (FWHM) denotes the half-height breadth of the resonant peak [8].

$$S = \frac{\Delta f}{\Delta n} \quad (16)$$

$$Q = \frac{f_T}{FWHM} \quad (17)$$

$$FOM = \frac{S}{FWHM} \quad (18)$$

$$DL = \frac{f_T}{20 \cdot S \cdot Q} \quad (19)$$

### 2.3.1. Forward scale for detection

RI and  $\theta$  can be detected in the forward scale. In Figure 8(a), it can be seen intuitively that with the change of RI from 3.85 to 3.97 the AP appears as a blue-shift phenomenon that is able to be detected biological elements such as galena. This is mainly because the AP is dependent on the RI of the medium. When the RI changes, the wave vector and phase will

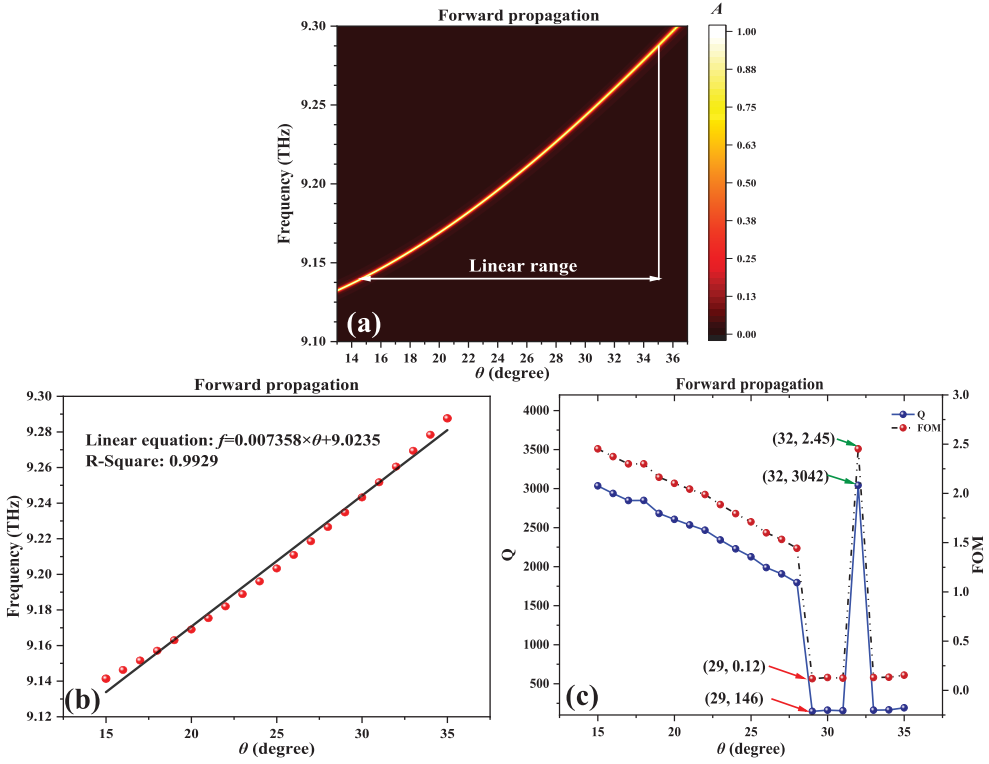


**Figure 9.** (a) The corresponding three-dimensional overhead plan for  $\theta$ , (b) Linear relationship between  $\theta$  and frequency (c)  $Q$  and FOM change with  $\theta$ .

be affected and the resonant frequency will be changed. From the 3-D top view, in the linear range, the AP value is always greater than 0.9, which ensures excellent detection performance. Figure 8(b) shows the linear fitting equation between  $n_A$  and frequency. The linear equation is  $f = -1.1773 \times n_A + 13.64$ , where  $S = -1.1773$  THz/RIU. The value of R-Square is a measure of the degree of linear fitting, and the closer the value is to 1, the better the line type fitting. Here, the R-Square is 0.9964. This indicates that the linearity of RI and frequency is very high, and the response on the device shows perfect detection performance. In Figure 8(c), the curves of  $Q$  and FOM variation with frequency are plotted. The maximum values of  $Q$  and FOM are 8265 and 1070  $\text{RIU}^{-1}$  when the  $n_A$  is 3.865, which is an excellent value for detection. The overall trends of  $Q$  and FOM are to decrease with the increase of RI, and the minimum values are 6405 and 841  $\text{RIU}^{-1}$  when  $n_A$  is equal to 3.97, respectively. But this can still achieve good performance for detection.

Angle detection is quite an important dimension for detection devices. This LPS can also realize the detection of  $\theta$ . As shown in Figure 9(a), in the range of  $15^\circ$  to  $35^\circ$ , with the increase of the  $\theta$ , the AP is blue-shifted, which is opposite to the situation when measuring the RI. In Figure 9(b), the linear fitting equation between  $\theta$  and frequency is  $f = 0.007358 \times \theta + 9.0236$  and the R-Square can be 0.9929, which satisfies the requirements of detection. After further calculations, the maximum  $Q$  and FOM of this LPS are obtained as 3042 and 2.45  $\text{degree}^{-1}$  under  $S = 0.007358$  THz/RIU when  $\theta = 32^\circ$ . Moreover, in Figure 9(c), it can be observed

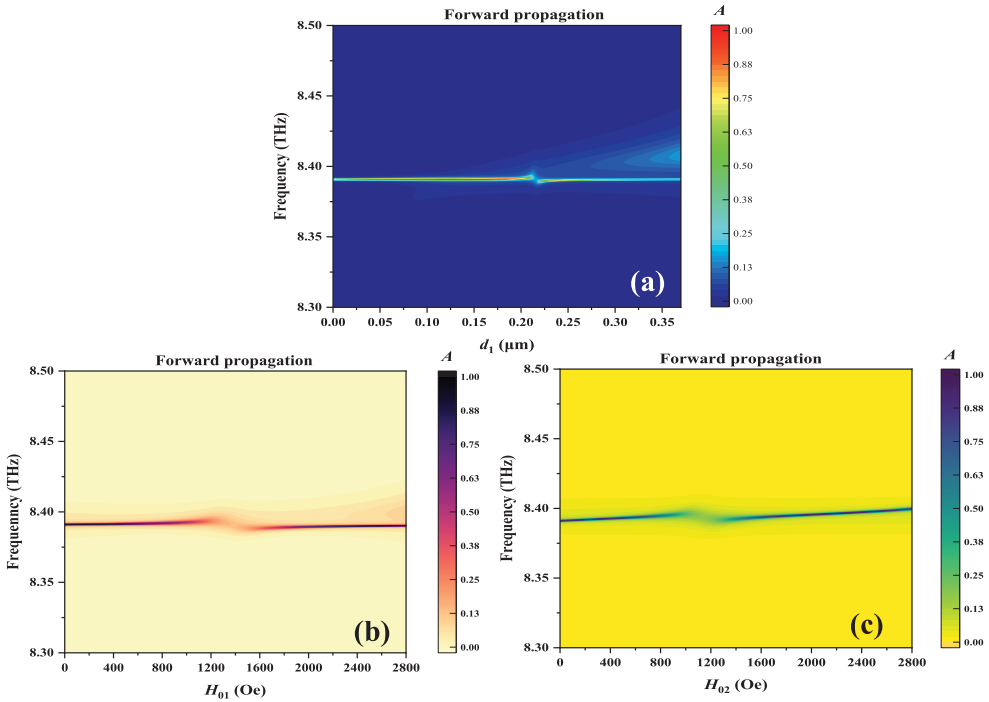


**Figure 10.** Top view of  $A$  change with frequency and (a)  $d_1$ , (b)  $H_{01}$ , and (c)  $H_{02}$ .

that Q and FOM are to decrease sharply with the increase of  $\theta$  from 3042 to 161 within the area of  $15^\circ$  to  $35^\circ$ .

However, the physical quantities  $Ri$ ,  $H_{01}$ , and  $H_{02}$  that can be detected in the backward direction do not have good performance in forward detection. The following is a more detailed discussion. With the NOR logical gate frequency point as the center, the selected frequency range is 8.30 THz  $\sim$  8.50 THz. In Figure 10(a), when the  $d_1$  increases, the frequency of the AP does not shift significantly, which is located about frequency = 8.391 THz. It means that the value of  $S$  can be 0. Meanwhile, the  $A$  is much less than 0.1 when  $d_1 = 0.22 \mu\text{m}$ , while this performance is far from the basic requirements of the detection. In Figure 10(b), the situation is the same as in Figure 10(a). The position of AP does not move and the  $A$  drops to almost 0 when the  $H_{01} = 0.14 \text{ T}$ . As shown in Figure 10(c), compared with the first two cases, the frequency moves to a high frequency when the  $H_{02}$  increases from 0 T to 0.28 T. But in the process of increasing, there is a gap in the  $A$  as  $H_{02} = 0.11 \text{ T}$  which is a bad performance for detection. Another reason, as can be seen in Figure 10, is that the sensitivity is too poor. This can seriously affect the accuracy of the detection.

### 2.3.2. Backward scale for detection

The thickness of  $\text{YIG}_1$  ( $d_1$ ),  $H_{01}$ , and  $H_{02}$  can be detected on the backward scale. To begin with, the detection can be used to detect the thickness of  $\text{YIG}_1$  ( $d_1$ ). From the top view in Figure 11(a), the AP is blue-shift with the increase of  $d_1$ . At the same time, it can be clearly seen that the value of AP is always greater than 0.9 in the linear range from 0.5-3  $\mu\text{m}$ . The specific linear equation data analysis is presented in Figure 11(b). The linear equation is

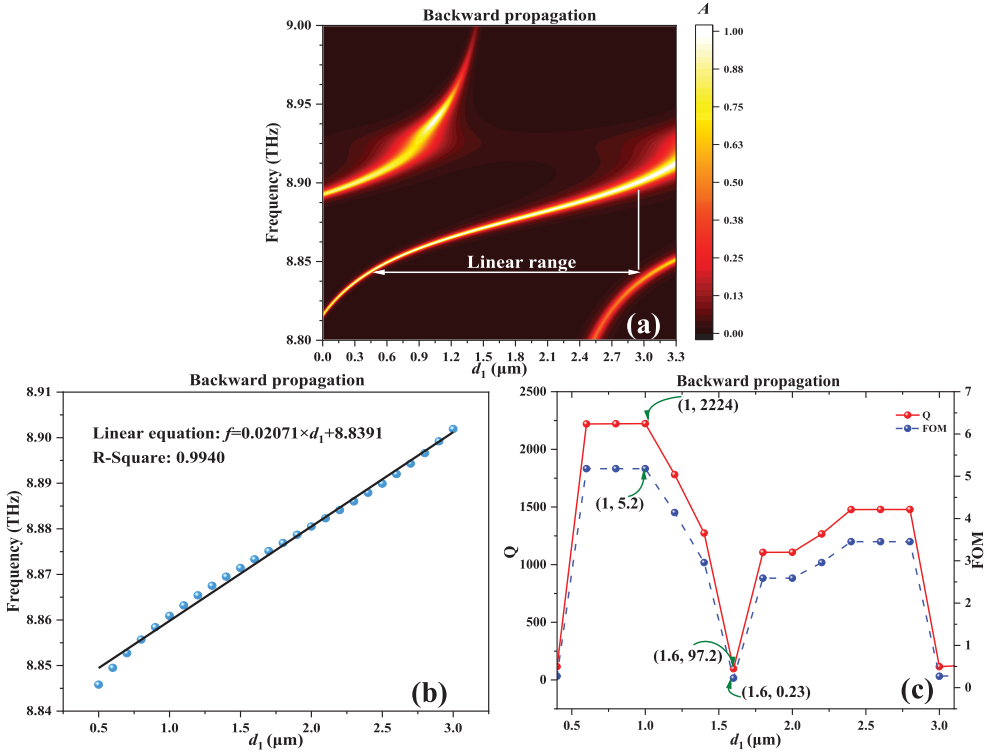


**Figure 11.** (a) The 3-D top view of the  $A$  change with  $d_1$  and frequency. (b) The formulation of linear fitting between  $d_1$  and frequency. (c)  $Q$  and FOM change with  $d_1$ .

$f = 0.02071 \times d_1 + 8.8391$  and R-Square is 0.994, which is a wonderful value for demonstrating the performance of detection. In the case of  $S = 0.02071 \text{ THz}/\mu\text{m}$ , the maximum  $Q$  and FOM are calculated to be 2223 and  $5.2 \mu\text{m}^{-1}$  when  $d_1 = 1 \mu\text{m}$ . From Figure 11(c), the minimum  $Q$  and FOM are 97.2 and  $0.23 \mu\text{m}^{-1}$  when  $d_1 = 1.6 \mu\text{m}$ . According to Eq(17), in the case of the same FWHM, the value of  $Q$  is limited to the selected frequency. Most  $Q$  values are more than 1000 in Figure 11(c) which attain the qualification of detection.

The detection of small changes in magnetic field intensity is quite important for the detection of precision magnetron devices, which is special for magnetic control logical operation. Below, the detection range and performance of  $H_{01}$  and  $H_{02}$  will be discussed. In the 3-D top view in Figure 12(a), the vast majority of the  $A$  is higher than 0.9, and with the  $H_{01}$  of the change in amplitude does not decrease. Figure 12(b) shows the linear fitting equation of frequency versus  $H_{01}$ . From 8.88 THz to 8.90 THz, the linear region of the  $H_{01}$  variation is  $0 \sim 0.26 \text{ T}$ . The linear fitting equation between them is  $f = 0.06878 \times H_{01} + 8.8786$ ,  $S = 0.06872 \text{ THz/T}$  and R-Square is 0.9950, which confirms the requirement of detection. In Figure 12(c), the highest point of the  $Q$  and FOM are 3704 and  $28.6 \text{ T}^{-1}$  when  $H_{01}$  is 0.16 T. On the whole,  $Q$  and FOM are to rise first and then fall, reaching a minimum at  $H_{01} = 0.26 \text{ T}$ , where  $Q$  and FOM are equal to 2781 and 21.5, severally.

On the other hand, when the detection is used to measure the  $H_{02}$ , it also has an equally excellent performance. The pattern of the frequency shift of the AP is shown in Figure 13(a) as the  $H_{02}$  changes. In the range covered by the frequency, the change of  $H_{02}$  is from 0 to

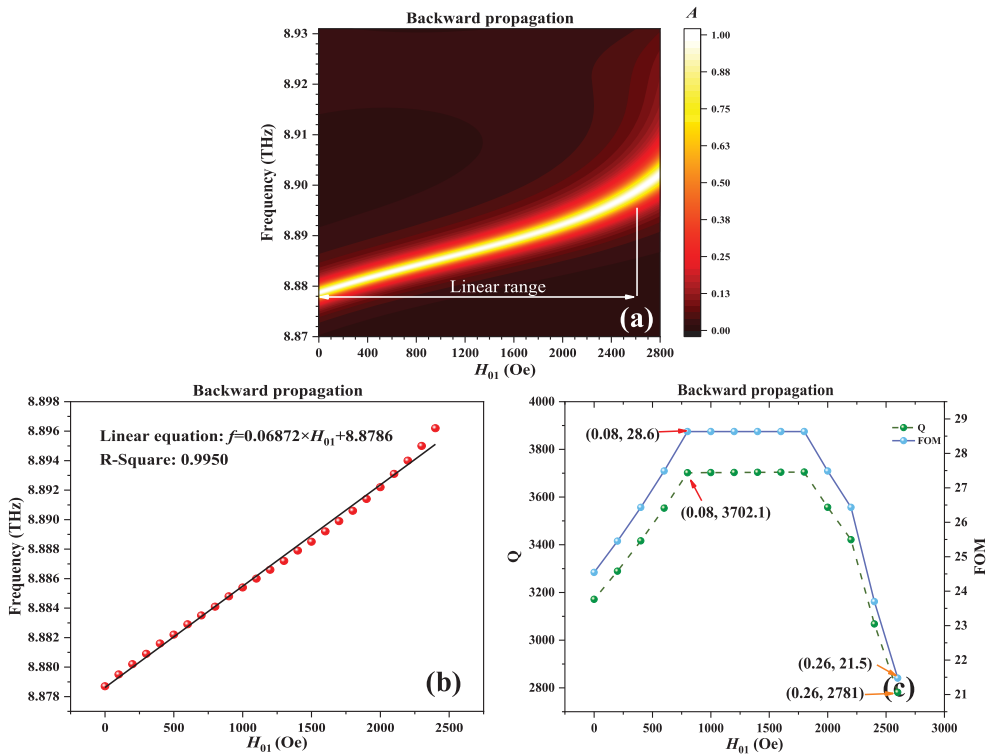


**Figure 12.** (a) The 3-D top view of the  $A$  vary with  $H_{01}$  and frequency. (b) The relationship between  $H_{01}$  and frequency. (c)  $Q$  and FOM variation with  $H_{01}$ .

0.26 T. The AP shown in the figure has an absorption amplitude greater than 0.9, and the amplitude does not decrease with the change of the AP position. The linear fit curves of  $H_{02}$  and frequency are shown in Figure 13(b). The linear fit curve when R-square = 0.9979 is  $f = 0.02689 \times H_{02} + 8.8788$ , which can be seen as highly linear and suitable for detection. The maximum  $Q$  and FOM are 3209 and  $10 \text{ T}^{-1}$  separately when the  $H_{02}$  is equal to 0.18 T. From Figure 13(c), to sum up,  $Q$  and FOM are first stable and then decreasing, with a minimum value of 2867 and  $8.7 \text{ T}^{-1}$  apart when  $H_{02} = 0.26 \text{ T}$ . In addition, since we have set a step size of 10 Oe, magnetic field detection is possible for a single-digit order of Oe. However, for smaller magnitudes, such as 0.1 Oe, the accuracy of detection may be limited by sensitivity.

Similarly, there are two physical quantities, which are RI and  $\theta$ , negative about detection in the backward propagation. In Figure 14(a), since the frequency point of the backward NOR logical gate is taken as the center, the frequency range varies from 8.80 THz to 9.00 THz. Though the AP is over 0.9, there still is a gap in the 3-D top view when RI is 3.90. When the  $\theta$  changes, the jump of AP is relatively large. To avoid double counting of AP, the frequency range is expanded to 9.2 THz in Figure 14(b). Meanwhile, despite the wonderful linear relationship, the AP is about 0.5 which is a poor value for detection. A gap appears when  $\theta$  is equal to 29. Considering the discussion above, only  $d_1$ ,  $H_{01}$ , and  $H_{02}$  are concerned with backward detection.

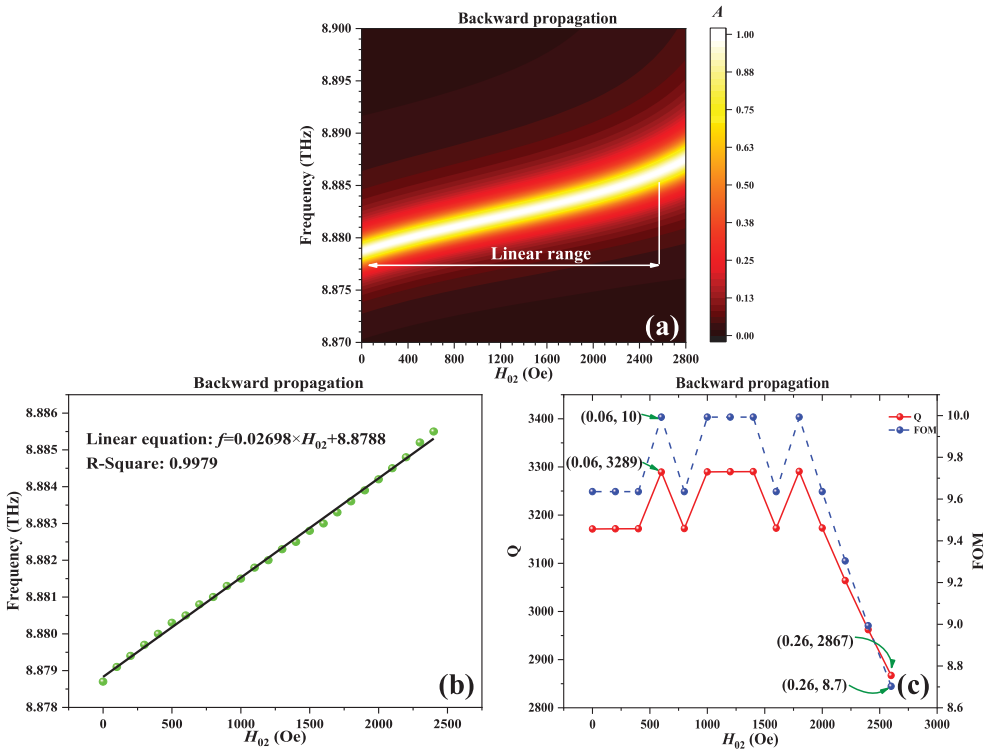


**Figure 13.** (a) The 3-D top view of the  $A$  vary with  $H_{02}$  and frequency. (b) The formulation of  $H_{02}$  and frequency. (c)  $Q$  and FOM change with  $H_{02}$ .

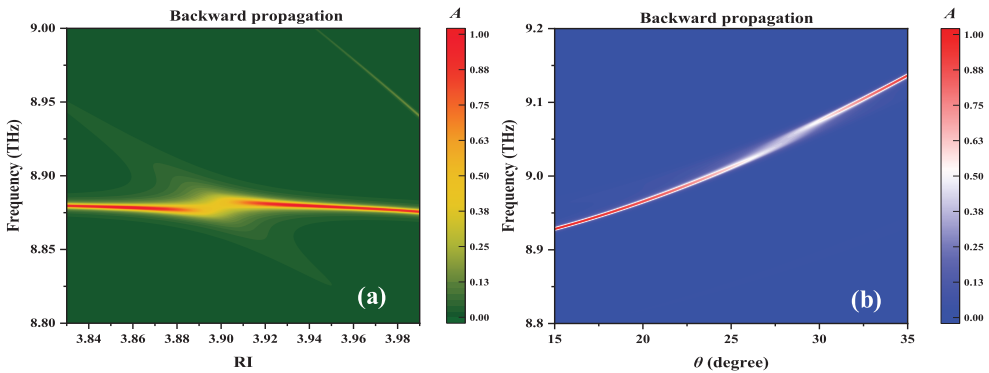


**Figure 14.** The corresponding 3-D overhead plan for (a) RI, and (b)  $\theta$ .

Moreover, as shown in Table 2, the forward and backward optimal performance of the LPS is compared with the optimal performance of the logic gate or detector in the report, and it is found that the proposed LPS has better performance in several aspects.

It is worth stating that the physical quantities detected in the forward direction are found to be not fully uniform with those detected in the backward direction. This is due to the fact that the PT-symmetry of the structure is broken and the EWs do not produce exactly



**Table 2.** Comparison of performance between this work and published reported.

References	Physical quantity	LR	S	FOM	Logic operation
[8]	Magnetic field	None	None	None	None
	Thickness	None	None	None	
	Incidence angle	None	None	None	
	Refractive index	1 ~ 3.5	1.58 THz/RIU	$3.6 \times 10^5 \text{ RIU}^{-1}$	
[26]	Magnetic field	None	None	None	None
	Thickness	None	None	None	
	Incidence angle	None	None	None	
	Refractive index	1.45 ~ 1.46	28000 nm/RIU	None	
[33]	Magnetic field	1.9 T ~ 2.55 T	0.838 THz/T	$34.2 \text{ T}^{-1}$	None
	Thickness	None	None	None	
	Incidence angle	None	None	None	
	Refractive index	1.4 ~ 3.8	7.144 THz/RIU	$5656.7 \text{ RIU}^{-1}$	
[34]	Magnetic field	None	None	None	OR
	Thickness	None	None	None	
	Incidence angle	None	None	None	
	Refractive index	None	None	None	
[28]	Magnetic field	$H_{01}: 1.14 \text{ T} \sim 1.40 \text{ T}$ $H_{02}: 1.20 \text{ T} \sim 1.45 \text{ T}$	0.528 THz/T 3.13 THz/T	$29 \text{ T}^{-1}$ $430 \text{ T}^{-1}$	AND
	Thickness	None	None	None	
	Incidence angle	None	None	None	
	Refractive index	2.21 ~ 2.65	0.113 THz/RIU	$66.5 \text{ RIU}^{-1}$	
[35]	Magnetic field	0.2 T ~ 2.6 T	1.41 GHz/T	$30.65 \text{ T}^{-1}$	None
	Thickness	None	None	None	
	Incidence angle	$28^\circ \sim 78^\circ$	0.98 GHz/degree	$24.75 \text{ degree}^{-1}$	
	Refractive index	1.05 ~ 2.05	34.3 GHz/RIU	$634 \text{ RIU}^{-1}$	
This work	Magnetic field	$H_{01}: 0 \text{ T} \sim 0.26 \text{ T}$ $H_{02}: 0 \text{ T} \sim 0.26 \text{ T}$	0.06872 THz/T 0.02698 THz/T	$28.6 \text{ T}^{-1}$ $10 \text{ T}^{-1}$	NOR
	Thickness	$0.5 \mu\text{m} \sim 3 \mu\text{m}$	0.02071 THz/ $\mu\text{m}$	$5.2 \mu\text{m}^{-1}$	
	Incidence angle	$15^\circ \sim 35^\circ$	0.00754 THz/degree	$2.45 \text{ degree}^{-1}$	
	Refractive index	3.85 ~ 3.97	-1.1773 THz/RIU	$1070 \text{ RIU}^{-1}$	

the same properties from the forward incidence and the backward incidence. The forward direction produces an AP for the detection of RI, while the backward direction does not. The converse is also true. For this reason, excellent performance for multi-physics detection in a different direction is achieved.

### 3. Conclusions

In conclusion, it is suggested to design a LPS that integrates magnetic-controlled NOR logical operation, the detection of angle, YIG thickness, RI, and  $H_{01}$  and  $H_{02}$  magnetic fields of small changes. The transfer matrix approach is used to calculate the  $A$  of the structure. The targeted localization of the absorption peak can realize all functions. For the forward propagation, the angle and RI are  $15 \sim 35^\circ$ , and  $3.85 \sim 3.97$ , separately, and the maximum Q and FOM are 3042, 8264, and  $2.45 \text{ degree}^{-1}$ ,  $1070 \text{ RIU}^{-1}$ , apart. For the backward propagation, the  $H_{01}$ ,  $H_{02}$ , the thickness of YIG<sub>1</sub> are  $0 \sim 0.26 \text{ T}$ ,  $0 \sim 0.26 \text{ T}$ , and  $0.5 \sim 3 \mu\text{m}$ , the corresponding values are about 3704, 3290, 2223, 28.6,  $10 \text{ T}^{-1}$ , and  $5.2 \mu\text{m}^{-1}$ . The 1-D LPS presented in this paper has the function of NOR logical operation and detection at the forward and backward scales and will have application prospects in optical communication, optical processing, biological detection, and refractive index measurement of materials in the future.

## Acknowledgments

This work was supported by the National College Students Innovation and Entrepreneurship Training Program (Grant No. 202310293015Z).

## Disclosure statement

No potential conflict of interest was reported by the author(s).

## Funding

This work was supported by the National College Students Innovation and Entrepreneurship Training Program (Grant No. 202310293015Z).

## References

- [1] Gunyakov VA, Krakhalev MN, Timofeev IV, et al. Optical modes of multilayered photonic structure containing nematic layer with abnormal electroconvective rolls. *Opt Mater (Amst)*. 2020;100(3):109630. doi:10.1016/j.optmat.2019.109630
- [2] Padhy A, Bandyopadhyay R. Enhanced transmission induced by embedded graphene in periodic, quasiperiodic, and random photonic crystals. *J Opt Soc Am B*. 2020;37(12):3801–3808. doi:10.1364/JOSAB.402357
- [3] Ansari N, Mirbaghestan K. Design of wavelength-adjustable dual-narrowband absorber by photonic crystals With Two defects containing MoS<sub>2</sub> monolayer. *J Lightwave Technol*. 2020;38(23):6678–6684. doi:10.1109/JLT.2020.3015938
- [4] Alagappan G, Sun XW, Shum P. One-dimensional anisotropic photonic crystal with a tunable bandgap. *J Opt Soc Am B*. 2006;23(1):159–167. doi:10.1364/JOSAB.23.000159
- [5] Yang YP, Lin KC, Yang IC. All-optical photonic crystal AND gate with multiple operating wavelengths. *Opt Commun*. 2013;297:165–168. doi:10.1016/j.optcom.2013.01.035
- [6] Sfindla YL, He X, Harris GI, et al. *Frontiers in Optics*. 2020.
- [7] Ali MZ, Abdullah T. Properties of the angular gap in a one-dimensional photonic band gap structure containing single negative materials. *Phys Lett A*. 2008;372(10):1695–1700. doi:10.1016/j.physleta.2007.10.022
- [8] Zaky ZA, Ahmed AM, Shalaby AS. Re-epithelialization and immune cell behaviour in an ex vivo human skin model. *Sci Rep*. 2020;10(1):1–9. doi:10.1038/s41598-019-56847-4
- [9] Olyaei S, Dehghani AA. High resolution and wide dynamic range pressure sensor based on two-dimensional photonic crystal. *Photonic Sens*. 2012;2(1):92–96. doi:10.1007/s13320-011-0044-1
- [10] Yang YH, Chen CH, Chang JSF. Wide-field-of-view GaAs/AlxOy one-dimensional photonic crystal filter. *Appl Opt*. 2005;44(8):1503–1511. doi:10.1364/AO.44.001503
- [11] Sharma Y, Prasad S, Singh V. Dispersion behavior of electromagnetic wave near the resonance in 1D magnetized ferrite photonic crystals. *Opt Quantum Electron*. 2018;50(11):1–19. doi:10.1007/s11082-018-1677-8
- [12] Mazur J, Mrozowski M. Nonreciprocal operation of structures comprising a section of coupled ferrite lines with longitudinal magnetization. *IEEE Trans Microw Theory Tech*. 1989;37(6):1012–1020. doi:10.1109/22.25405
- [13] Mondal SK, Stadler BJ, H. Novel designs for integrating YIG/air photonic crystal slab polarizers with waveguide Faraday rotators. *IEEE Photonics Technol Lett*. 2005;17(1):127–129. doi:10.1109/LPT.2004.838156
- [14] Dmitriev V. Symmetry properties of 2D magnetic photonic crystals with square lattice. *The European Physical Journal Applied Physics*. 2005;32(3):159–165. doi:10.1051/epjap:2005087
- [15] Yang YJ, Wen YJ, Zhong GJ. Tunable broadband metamaterial absorber consisting of ferrite slabs and a copper wire. *Chin Phys B*. 2012;21(3):038501. doi:10.1088/1674-1056/21/3/038501

- [16] Fu JX, Lian J, Liu RJ. Unidirectional channel-drop filter by one-way gyromagnetic photonic crystal waveguides. *Appl Phys Lett*. 2011;98(21):211104. doi:10.1063/1.3593027
- [17] Bi K, Zhu W, Lei M, et al. Magnetically tunable wideband microwave filter using ferrite-based metamaterials. *Appl Phys Lett*. 2015;106(17):173507. doi:10.1063/1.4918992
- [18] Wang Y, Zhang D, Xu S, et al. Low-loss Y-junction two-dimensional magneto-photonic crystals circulator using a ferrite cylinder. *Opt Commun*. 2016;369:1–6. doi:10.1016/j.optcom.2016.02.019
- [19] Fan F, Chang SJ, Niu C, et al. Magnetically tunable silicon-ferrite photonic crystals for terahertz circulator. *Opt Commun*. 2012;285(18):3763–3769. doi:10.1016/j.optcom.2012.05.044
- [20] Chong YD, Ge L, Stone AD. PT-symmetry breaking and laser-absorber modes in optical scattering systems. *Phys Rev Lett*. 2011;106(9):093902. doi:10.1103/PhysRevLett.106.093902
- [21] Szameit A, Rechtsman MC, Bahat-Treidel O, et al. PT-symmetry in honeycomb photonic lattices. *Phys Rev A*. 2011;84(2):021806. doi:10.1103/PhysRevA.84.021806
- [22] Guo A, Salamo GJ, Duchesne D, et al. Observation of PT-symmetry breaking in complex optical potentials. *Phys Rev Lett*. 2009;103(9):093902. doi:10.1103/PhysRevLett.103.093902
- [23] Ruter C, Makris KG, El-Ganainy R, et al. Observation of parity–time symmetry in optics. *Nat Phys*. 2010;6(3):192–195. doi:10.1038/nphys1515
- [24] He L, Zhang WX, Zhang XD. Topological all-optical logic gates based on two-dimensional photonic crystals. *Opt Express*. 2019;27(18):25841–25859. doi:10.1364/OE.27.025841
- [25] Zou H, Liang GQ, Wang HZ. Efficient all-optical dual-channel switches, logic gates, half-adder, and half-subtractor in a one-dimensional photonic heterostructure. *J Opt Soc Am B*. 2008;25(3):351. doi:10.1364/JOSAB.25.000351
- [26] Wang Y, Li S, Li J, et al. High-sensitivity photonic crystal fiber refractive index sensor based on directional coupler. *Opt Fiber Technol*. 2019;49:16–21. doi:10.1016/j.yofte.2019.01.015
- [27] Zhang Y, Wu FP, Zhang HF. Theoretical model of a RI THz sensor realized by coherent perfect absorption With optical phase modulation. *IEEE Sens J*. 2022;22(15):14842–14850. doi:10.1109/JSEN.2022.3182815
- [28] Rao SS, Zhang JT, Zhang HF. A multifunctional and multiscale device of magnetic-controlled AND logical operation and detection based on the nonreciprocity of the magnetized InSb photonic structure. *Results Phys*. 2021;31:105058. doi:10.1016/j.rinp.2021.105058
- [29] Ma Y, Zhang HF. Wide-angle energy steering and magnetic information detection-coding of stacked ferrite-based elements in the gradient magnetic domain. *Opt Laser Technol*. 2022;156:108544. doi:10.1016/j.optlastec.2022.108544
- [30] Guo SJ, Li ZJ, Li FY, et al. The asymmetric optical bistability based on the one-dimensional photonic crystals composed of the defect layers containing the magnetized ferrite and nonlinear kerr dielectric under the transverse electric polarization. *J Appl Phys*. 2021;129(9):093104. doi:10.1063/5.0041461
- [31] Qi L, Yang Z, Lan F, et al. Properties of obliquely incident electromagnetic wave in one-dimensional magnetized plasma photonic crystals. *Phys Plasmas*. 2010;17(4):042501. doi:10.1063/1.3360296
- [32] Mehdian H, Mohammadzahery Z, Hasanbeigi A. Optical and magneto-optical properties of plasma-magnetic metamaterials. *J Phys D: Appl Phys*. 2015;48(30):305101. doi:10.1088/0022-3727/48/30/305101
- [33] Rao SS, Liu YM, Wan BF, et al. Theoretical proposal of a multitasking sensor realized by the mechanism of nonreciprocal absorption evanescent wave in the magnetized ferrite photonic crystals. *IEEE Sens J*. 2021;21(24):27405–27413. doi:10.1109/JSEN.2021.3126158
- [34] Pirzadi M, Mir A, Bodaghi D. Realization of ultra-accurate and compact All-optical photonic crystal OR logic gate. *IEEE Photonics Technol Lett*. 2016;28(21):2387–2390. doi:10.1109/LPT.2016.2596580
- [35] Wan BF, Xu Y, Zhou ZW, et al. Theoretical investigation of a sensor based on One-dimensional photonic crystals to measure four physical quantities. *IEEE Sens J*. 2021;21(3):2846–2853. doi:10.1109/JSEN.2020.3027759